Creep and quakes on the northern transition zone of the San Andreas fault from GPS and InSAR data

I. A. Johanson, R. Bürgmann

Department of Earth and Planetary Science, University of California, Berkeley, CA, USA

The San Juan Bautista (SJB) segment forms the northern transition zone of the creeping section of the San Andreas fault. It is an area of moderate seismicity; the largest instrumentally-recorded earthquakes have been M≤5.5. However, historic records suggest six M≥6 earthquakes occurred near the SJB segment between 1840 and 1899. It is also an area that has experienced several slow earthquakes. We perform a joint inversion of GPS and InSAR data to determine the current rate and distribution of interseismic creep. We find two low-slip/locked segments at mid-seismogenic depths that may represent source regions for the 19th century earthquakes. We find that the SJB segment is currently accumulating strain energy at the rate of one M6.3 - 6.7 earthquake per century. At this rate, the 1840 - 1899 sequence released 135 - 510 years of accumulated moment deficit.

1. Introduction

Surface creep on the San Juan Bautista (SJB) segment has been studied since the **19**60's with both creepmeters and alignment array surveys (see *Bokelmann and Kovach* [2003] and *Galehouse and Lienkaemper* [2003] for summaries). These creepmeter records include observations of episodic creep. Episodic creep events take place over hours to days and involve slip in the upper 500 m of the fault [*Gladwin et al.*, 1994]. In 1992, a slow earthquake was detected **on the SJB segment** by creepmeters and strainmeters. This event occurred in the same section of the fault as the episodic creep, but involved transient slip down to a depth of 4 - 8 km [*Linde et al.*, 1996]. Further slow earthquakes **have occurred** in 1996, 1998, 2003 and 2004, with equivalent magnitudes of M$_w$∼5, and on time scales **of weeks** [*Gwyther et al.*, 2000; *Bilham et al.*, 2004; *Gladwin*, 2004]. A change in creep rates has been observed in response to the 1989 Loma Prieta earthquake. Surface creep rates significantly accelerated along the SJB segment and have not returned to pre-earthquake levels [*Behr et al.*, 1997; *Bokelmann and Kovach*, 2003].

The largest recent earthquake on the SJB segment was a M$_w$5.1 event which **immediately preceded** the 1998 slow earthquake [*Gwyther et al.*, 2000; *Uhrhammer et al.*, 1999]. However, historic records indicate that the SJB segment produced a series of six M≥6 earthquakes between 1840 and 1899 [*Toppozada*, 2000; *Toppozada et al.*, 2002]. Since then, *Toppozada et al.* [2000] report only two M5.8 earthquakes in 1910 and 1916 in the same area. Given the history of slip transients in the SJB area, does **seismic quiescence of the 20th century, relative to the 19th century** indicate a **long time**-scale **increase** in creep rates? **Which**

could occur perhaps in response to increased stress on the SJB segment from the 1906 San Francisco earthquake. In this study, we use a decade of GPS and SAR data to determine the distribution and rate of creep at the depths of the largest slow earthquakes and seismic events. The slip model illuminates the relationship between subsurface creep, slow earthquakes, and earthquakes. We estimate a slip budget for the SJB segment to determine if current creep conditions would allow a similar rate of large earthquake production as seen in the 19th century.

2. Data

2.1. GPS Data

We completed campaign GPS surveys in 2001, 2002, and 2003 on up to 50 benchmarks throughout the southern Bay Area. These benchmarks had previous observations from as far back as 1994. The data is processed in GAMIT together with BARD and IGS stations to produce daily unconstrained solutions. The daily solutions are combined with data from throughout the San Francisco Bay Area in the BAVU dataset [*d'Alessio et al.*, 2005] and stabilized in a North American reference frame using GLOBK. More detail on the data and data processing is available in *d'Alessio et al.* [2005]. The GPS velocities (and InSAR range-change rate samples) used in this study are available in the auxiliary materials[1].

2.2. InSAR Data
2.2.1. Interferogram processing

We complement the high-precision GPS velocities with high-spatial-resolution InSAR range-change rates. **Range-change refers to the change in line-of-sight distance between the satellite and the ground.** A set of 10 ERS1 & ERS2 scenes were processed using the ROI_Pac software developed at JPL. **The contribution of topography to the interferogram phase was removed using** a USGS 30 m DEM. ROI_Pac re-estimates satellite orbit parameters by fitting and removing a low-order polynomial from the interferogram phase data. We preserve the phase gradient due to regional deformation by removing a GPS derived model of interseismic deformation before orbit parameter re-estimation and replacing it after phase unwrapping. Phase unwrapping was performed using SNAPhU [*Chen and Zebker*, 2001] **. In InSAR processing, areas which have poor spatial coherence (speckle) cannot be unwrapped. SNAPhU uses a cost threshold to determine which areas of the interferogram can be unwrapped; pixels with cost above this threshold are removed from the final product. We specified a cost threshold of 300, which** produces similar results to masking out areas with a spatial correlation coefficient **of** less than 0.1. The interferograms are **georeferenced** using the USGS DEM and resampled to 30 m spacing using a nearest neighbor method.

2.2.2. Stacking and sampling

---

[1]Auxiliary material and data tables are available at ftp://ftp.agu.org/apend/gl/ARTICLENUMBER

The challenge in applying InSAR data to study interseismic deformation is that the tectonic signal is generally very small, producing less than one phase cycle of range-change per year, and is easily obscured by atmospheric delay errors [**Wright et al., 2001**]. Furthermore, in the San Juan Bautista area, interferometric pairs spanning more than a year suffer from severe **temporal** decorrelation**, leading to poor spatial coherence and little unwrapped signal.** We **address both of these problems by stacking** together short time-span pairs**. Interferogram stacking is generally used to mitigate atmospheric delay errors by averaging the input interferograms [Zebker et al., 1997]. We choose our input interferograms** such that the **ending** scene in one pair is the **beginning** scene in the next (Table 1). **With this selection method, atmospheric errors from repeated dates cancel eachother and the stack** reproduces the benefits of a long time-span interferogram. We use nine pairs, all spanning less than two years, to produce a stack that is equivalent to a single 5.75 year interferogram.

The nine **georeferenced** interferograms are added together and scaled by the total time span to produce a map of yearly range-change rates (Figure 1). **Areas which could not be unwrapped in any single interferogram were not included in the final stack.** The stack is subsampled to reduce the number of observations to a computationally tenable number and to account for correlations between samples introduced by filtering, resampling to the DEM spacing and by any remaining atmospheric errors. Within a 75 x 25 km box around the SJB segment, we **sample the data on a grid with 500 meter spacing**; outside this box we sample on a 2 km grid. The denser near-fault spacing increases our resolution on the SJB segment, while the sparser far-field spacing provides information on the regional fault system. Because the actual uncertainties in the InSAR data are not well known, we estimate them from the variance of the 25 pixel values averaged within each sample.

2.2.3. Non-tectonic, Vertical Motion

The Hollister/San Juan valley basin (Figure 1) demonstrates vertical motions associated with groundwater movement. We use only one satellite configuration (descending orbit) and so cannot uniquely isolate non-tectonic vertical motion in the InSAR data. Groundwater-induced vertical motion is the result of expansion and compaction of unconsolidated sediment; therefore we remove all InSAR data points which occur on Quaternary sediments (as identified by *Jennings* [1977]) from our model inversions. This conservative method removes both the data influenced by non-tectonic motion in the Hollister/San Juan valley and any other as yet unidentified area susceptible to groundwater-induced vertical motion.

3. Model Formulation

We formulate our inversion using the equations of *Okada* [1985] for deformation at the surface of a homogeneous, isotropic, elastic half-space due to slip on embedded dislocations. Deep dislocations (below locking depth **to 3000 km**) simulate strain accumulation on the regional fault system, including the San Andreas, Calaveras, Paicines, Sargent and Hayward faults (see auxiliary materials, Figure S3). Shallow dislocations (above locking depth) are included on the Calaveras fault and the SJB and Santa Cruz segments of the San Andreas fault. We base our choice of locking depth on the estimates **of D95** by *d'Alessio et al.* [2005], **which is** based on the depth distribution of seismicity and surface heat flow data. The shallow San Andreas fault along the SJB segment and a portion of the Santa Cruz segment to the north is discretized into 174 2.5x1.5 km elements. The

strike of each element in the top two rows closely matches the mapped surface trace of the San Andreas fault, while the deeper elements match only larger changes in strike. We set up our inversion using the method of *Price and Bürgmann* [2002], such that we solve the following equation for optimal slip rate values that minimize the weighted residual sum of squares while seeking a smooth slip rate distribution on the discretized shallow sections of the San Andreas fault.

$$\begin{bmatrix} \mathbf{W}_g \mathbf{G}_g \\ \alpha \mathbf{W}_s \mathbf{G}_s \\ \beta \nabla^2 \end{bmatrix}^{-1} \begin{bmatrix} \mathbf{W}_g \overrightarrow{\mathbf{d}}_g \\ \alpha \mathbf{W}_s \overrightarrow{\mathbf{d}}_s \\ \mathbf{0} \end{bmatrix} = \begin{bmatrix} \overrightarrow{\mathbf{s}} \\ \overrightarrow{\mathbf{t}} \end{bmatrix}$$

$\overrightarrow{\mathbf{d}}_g$ is the vector of GPS velocities in the east and north directions and $\overrightarrow{\mathbf{d}}_s$ contains the InSAR range-change rate samples. $\mathbf{G}_g$ and $\mathbf{G}_s$ are the design matrices of Greens functions, which relate unit slip on each dislocation to displacements or range-change at each observation point. $\mathbf{G}_s$ also contains elements to solve for an offset and linear slope ($\overrightarrow{\mathbf{t}}$) **to further compensate for residual errors in the satellite orbit parameters that would result in a phase gradient** across the InSAR stack. The data and design matrices are internally weighted by the inverse covariance matrix (χ^{-1}) such that

$$\mathbf{W}_{g/s}^T \mathbf{W}_{g/s} = \chi_{g/s}^{-1}$$

α weights the entire InSAR dataset relative to the GPS data. We choose $\alpha = 1.85$, which gives similar **weighted residual sum of squares** (WRSS) for each data set (518 and 556 for the GPS and InSAR data respectively). We apply a positivity constraint to all dislocations using a bounded variable least squares algorithm [*Stark and Parker*, 1995] and impose a slip rate of 35 mm/yr **(similar the maximum creep rate observed by Burford and Harsh [1980])** on the deep creeping section to compensate for sparse data coverage in that area. β is the weight given to the Laplacian smoothing operator (∇^2)**, which was applied to only the discretized elements in the SJB area**. β was chosen by examining a trade-off curve of roughness vs. WRSS for joint inversions and then choosing a value that provides as smooth a result as possible without greatly increasing the WRSS (Figure S1). Model fits are shown in Figure 2 and Figure S2.

4. Results and Discussion

4.1. San Juan Bautista Creep Distribution

4.1.1. Relationship to seismicity

Our model resolves 19.9 ± 1.4 mm/yr of creep on the shallow creeping section, decreasing **gradually** to the north **within the discretized SJB segments**. 12 km north of XSJ2 (Figure 3), the majority of the fault surface is locked, including the source area of the 1990 Chittenden earthquake sequence. Two low-creep/locked asperities occur at mid-seismogenic depths (asperities A and B in Figure 3), which may be source regions for moderate to large earthquakes. **The 1998 $M_w 5.1$ San Juan Bautista earthquake (which immediately preceded the 1998 slow earthquake) occurred within a microseismically active area just below asperity B.** The decrease in subsurface creep north of the creeping section into asperity B corresponds well with an area of little microseismicity. Similarly, the depth of the bottom edge of asperity B also matches well with the depth where microseismic activity occurs in this area. This supports the idea that on creeping faults there is an inverse relationship between microseismicity and locked, earthquake-producing asperities. However, asperity

A of our model shows a lack of inferred creep within a microseismically active area.

4.1.2. Relationship to slow earthquakes

Two slow earthquakes occurred on the SJB segment during the time spanned by our GPS and InSAR data. The slip from these slow earthquakes is averaged into our yearly slip rates. Nonetheless, the contributions from these events are not enough to account for all of the creep in the model elements in which they occur. **The 1998 slow earthquake contributes 3.5 mm/yr to the modeled secular rates in the elements in which it occurs and the 1996 slow earthquake contributes even less.** The rupture areas of the 1996 and 1998 slow earthquakes were estimated by *Gwyther et al.* [2000] from strainmeter records and are shown in Figure 3. The 1996 slow earthquake occurred on a creeping portion of the fault, between asperity A and the northern terminus. The 1998 slow earthquake slipped 20 mm at the edge of asperity B. A 1992 slow earthquake that preceded our observations occurred in between asperities A and B in an area of currently active creep. The locations of the slow earthquakes are consistent with previous observations in the Cascadia subduction zone that **show** slow earthquakes **to** occur in creeping areas of the fault near the locked plate interface rather than slipping otherwise locked sections [*Dragert et al.*, 2001].

4.2. Moment Deficit on the San Juan Bautista Segment

We seek to determine whether a sequence of earthquakes, similar to that seen in the 19th century, could occur on the SJB segment under its current creep conditions. We consider six earthquakes from the catalog of *Toppozada et al.* [2000] that locate within 5 km of the SJB segment surface trace. There is significant uncertainty in the locations of these events, such that some may, in fact, have occurred on **either** the adjoining Santa Cruz segment, the Calaveras **Fault** or the Paicines Fault [*Toppozada et al.*, 2002]. We calculate moment deficit rates for the $i = 114$ model elements in the shallow SJB segment (large red box in Figure 3) using

$$\dot{M}_{o(deficit)} = \sum_i \mu A_i \left(\dot{s}_{lt} - \dot{s}_i \right)$$

We must first establish the long-term slip rate ($\dot{s}_{lt}$) on this segment. **In our inversion we also** solve for a single deep slip rate on the SJB segment and the Santa Cruz segment to the north **(Figure 3)**. The joint inversion resolves 23.3 mm/yr of deep slip, whereas a GPS-only inversion resolves 16.8 mm/yr. Both of these rates are close to the expected range for the peninsular San Andreas fault [*Hall et al.*, 1999], so we perform the moment deficit calculations twice, using each of these rates. We also perform the calculations for two values of rigidity (μ), 15 and 25 GPa, **reflecting the seismic velocity contrast across the San Andreas fault in this area** [*Dorbath et al.*, 1996]. We report the lowest and highest deficit rates from this set of input parameters.

The shallow SJB segment creeps at an average rate of 11.7 mm/yr, which leaves 5.1 - 11.5 mm/yr of slip deficit and a moment deficit rate of $\mathbf{3.3 \times 10^{23} - 1.2 \times 10^{24}}$ **dyne·cm/yr**. At this rate the region could produce one M_w6.3 - 6.7 earthquake every century and it would take 135 - 510 years to accumulate the moment released in the 19th century sequence $\mathbf{(1.7 \times 10^{26}}$**dyne·cm over 60 years)**. Each of the two asperities could produce a M_w≈6 event every century. The large uncertainties in the historic earthquake locations do not allow us to definitively assign them to a particular asperity. That the 19th century sequence released hundreds of years worth of accumulated slip deficit is consistent with the relative quiescence observed in the 20th

century, **and does not indicate increased creep rates**. Our data samples post-Loma Prieta creep rates; pre-Loma Prieta surface creep rates were as much as 30% lower [*Bokelmann and Kovach*, 2003]. At 30% lower creep rates the 19th century earthquake sequence would still represent 105 - 300 years of moment accumulation.

It is interesting that the historic earthquakes occurred as a clustered sequence rather than a relatively regular series, such as is observed on the Parkfield segment. The Parkfield segment is similarly located at the southern end of the creeping section and is partially locked along a ∼25 km-long transition zone [*Murray and Segall*, 2002]. Based on our results, the ∼50 km-long SJB segment could produce a Parkfield-like event (M_w6.0) every 10 - 38 years, a similar repeat time to that found by *Murray and Segall* [2002] of 7 - 21 years for the Parkfield segment. Unlike Parkfield, the SJB segment is divided into two asperities surrounded by **creep**. *Toppozada* [2000] notes that the historic events all occurred close in time to either the 1838 M7.4 or the 1906 M7.8 earthquakes on the San Andreas fault**(both with southern terminations at San Juan Bautista)** suggesting that this segment is sensitive to changes in input stress from nearby earthquakes. **Rather than indicating increased creep rates, the current quiescence could be associated with a decrease in aseismic slip on the fault area surrounding the isolated asperities. The years following the 1838 earthquake and before the 1906 earthquake may have been periods of increased creep on the SJB segment, which increased the loading rate on the asperities.** [*Ben-Zion et al.*, 1993].

5. Conclusions

Historic records suggest a series of 19th century M≥6 earthquakes in the San Juan Bautista area. While there is significant uncertainty in the location of historic earthquakes, the number of large events attributed to this segment stands in contrast to the instrumentally observed seismicity. Our study shows that given the current distribution of creep, the SJB segment is accumulating a moment deficit at the rate of one M_w6.3 - 6.7 earthquake per century. Our model shows two separate low-creep/locked asperities, which could rupture independently of each other. The loading rate is similar to that seen on the Parkfield segment, but the SJB segment does not experience regularly occurring M_w6 earthquakes. Instead the segment appears to release centuries worth of strain accumulation in clusters that span decades and in response to stress changes from larger events.

References

Behr, J., R. Bilham, P. Bodin, K. S. Breckenridge, and A. G. Sylvester (1997), Increased surface creep rates on the San Andreas fault southeast of the Loma Prieta main shock, *U. S. Geol. Survey Prof. Paper 1550-D*, pp. D179–D192.

Ben-Zion, Y., J. R. Rice, and R. Dmowska (1993), Interaction of the San Andreas fault creeping segment with adjacent great rupture zones and earthquake recurrence at Parkfield, *J. Geophys. Res.*, *98*(B2), 2135–2144.

Bilham, R., N. Suszek, and S. Pinkney (2004), California creepmeters, *Seismol. Res. Lett.*, *75*(4), 481–492.

Bokelmann, G. H. R., and R. L. Kovach (2003), Long-term creep-rate changes and their causes, *Geophys. Res. Lett.*, *30*(8), 1445.

Burford, R. O., and P. W. Harsh (1980), Slip on the San Andreas fault in central California from alignment array surveys, *Bull. Seismol. Soc. Am.*, *70*(4), 1233–1261.

Chen, C. W., and H. A. Zebker (2001), Two-dimensional phase unwrapping with use of statistical models for cost functions in nonlinear optimization, *J. Opt. Soc. Am. A-Optics & Image Science*, *18*(2), 338–351.

d'Alessio, M., I. A. Johanson, R. Bürgmann, D. A. Schmidt, and M. H. Murray (2005), Slicing up the San Francisco Bay Area: Block kinematics and fault slip rates from GPS-derived surface velocites, *J. Geophys. Res.*, doi:10.1029/2004JB003496, in Press.

Dorbath, C., D. Oppenheimer, F. Amelung, and G. King (1996), Seismic tomography and deformation modeling of the junction of the San Andreas and Calaveras faults, *J. Geophys. Res.*, *101*(B12), 27,917–27,941.

Dragert, H., K. Wang, and T. S. James (2001), A silent slip event on the deeper Cascadia subduction interface, *Science*, *292*(5521), 1525–1528.

Galehouse, J. S., and J. J. Lienkaemper (2003), Inferences drawn from two decades of alinement array measurements of creep on faults in the San Francisco Bay region, *Bull. Seismol. Soc. Am.*, *93*(6), 2415–2433.

Gladwin, M. T. (2004), Maintenance, data archive and analysis of existing low-frequency GTSM installations in California, *NEHRP Annual Project Summary*, U. S. Geol. Survey.

Gladwin, M. T., R. L. Gwyther, R. H. G. Hart, and K. S. Breckenridge (1994), Measurements of the strain field associated with episodic creep events on the San Andreas fault at San Juan Bautista, California, *J. Geophys. Res.*, *99*(B3), 4559–4565.

Gwyther, R. L., C. H. Thurber, M. T. Gladwin, and M. Mee (2000), Seismic and aseismic observations of the 12th August 1998 San Juan Bautista, California M5.3 earthquake, in *3rd San Andreas Fault Conference*, pp. 209–213, Stanford University.

Hall, N. T., R. H. Wright, and K. B. Clahan (1999), Paleoseismic studies of the San Francisco Peninsula segment of the San Andreas fault zone near Woodside, California, *J. Geophys. Res.*, *104*(B10), 23,215–23,236.

Jennings, C. (1977), Geologic map of California, *Geologic Data Map Series*, California Department of Conservation, Division of Mines and Geology.

Linde, A. T., M. T. Gladwin, M. J. S. Johnston, R. L. Gwyther, and R. G. Bilham (1996), A slow earthquake sequence on the San Andreas fault, *Nature*, *383*(6595), 65–68.

Murray, J., and P. Segall (2002), Testing time-predictable earthquake recurrence by direct measurement of strain accumulation and release, *Nature*, *419*(6904), 287–291.

Okada, Y. (1985), Surface deformation due to shear and tensile faults in a half-space, *Bull. Seismol. Soc. Am.*, *75*(4), 1135–1154.

Price, E. J., and R. Bürgmann (2002), Interactions between the Landers and Hector Mine, California, earthquakes from space geodesy, boundary element modeling, and time-dependent friction, *Bull. Seismol. Soc. Am.*, *92*(4), 1450–1469.

Stark, P. B., and R. L. Parker (1995), Bounded-variable least-squares - an algorithm and applications, *Computation Stat.*, *10*(2), 129–141.

Toppozada, T. R. (2000), San Andreas M ≥ 5.5 earthquakes from Parkfield to Fort Bragg, California, 1800-1999, in *3rd San Andreas Fault Conference*, vol. 21, pp. 93–105, Stanford University.

Toppozada, T. R., D. M. Branum, M. Peterson, C. Hallstrom, C. Cramer, and M. Reichle (2000), Epicenters of and areas damaged by M ≥ 5 California earthquakes, 1800-1999, Map sheet 49, Calif. Div. Mines Geol.

Toppozada, T. R., D. M. Branum, M. S. Reichle, and C. L. Hallstrom (2002), San Andreas fault zone, California: M ≥ 5.5 earthquake history, *Bull. Seismol. Soc. Am.*, *92*(7), 2555–2601.

Uhrhammer, R., L. S. Gee, M. H. Murray, D. Dreger, and B. Romanowicz (1999), The Mw 5.1 San Juan Bautista, California earthquake of 12 August 1998, *Seismol. Res. Lett.*, *70*(1).

Waldhauser, F., and W. L. Ellsworth (1999), A double difference earthquake location algorithm; method and application to the San Andreas and Hayward faults, California, *EOS, Trans. AGU*, *80*(46), 705.

Wright, T., B. Parsons, and E. Fielding (2001), Measurement of interseismic strain accumulation across the North Anatolian Fault by satellite radar interferometry, *Geophys. Res. Lett.*, *28*(10), 2117–2120.

Zebker, H. A., P. A. Rosen, and S. Hensley (1997), Atmospheric effects in interferometric synthetic aperture radar surface deformation and topographic maps, *J. Geophys. Res.*, *102*(B4), 7547–7563.

I. A. Johanson and R. Bürgmann, Department of Earth and Planetary Science, University of California, Berkeley, 307 McCone Hall, Berkeley, CA, 94720, USA. (ingrid@seismo.berkeley.edu)

Table 1. Component interferograms for stack from ERS 1 & 2 data on track 299, shifted frame 2861

Begin Date	End Date	⊥Baseline (m)	Δtime (yrs)
8/13/95	5/19/96	47	0.77
5/19/96	5/20/96	80	0.00
5/20/96	6/24/96	88	0.10
6/24/96	7/14/97	78	1.05
7/14/97	8/18/97	-267	0.10
8/18/97	10/12/98	-70	1.15
10/12/98	11/1/99	-12	1.05
11/1/99	8/7/00	-79	0.77
8/7/00	5/14/01	-39	0.77
	Total time span		5.75

Figure 1. InSAR stack from data spanning 5.75 years, scaled to yearly rate. White circles outline the Hollister and Santa Clara Valley Basins where groundwater recharge results in non-tectonic vertical motion. These and other areas located on Quaternary sediment were removed before the model inversion (see section 2.2.3). White triangle is the location of creepmeter XSJ2, used as the origin for Figure 3.

Figure 2. Observed GPS velocities (grey arrows) with 95% confidence ellipses, and model fits to InSAR range change rates and GPS velocities (thinner purple arrows). GPS velocities are relative to station LUTZ (purple triangle).

Figure 3. Results of model inversion for slip on the discretized elements of the SJB segment. Cross-section is plotted looking north-eastward. Surface creep rates from line fits to creepmeter data from 1994-2001 are shown for comparison (colored triangles). The rupture areas for slow earthquakes in 1996 and 1998 are outlined in dashed grey lines [*Gwyther et al.*, 2000]. Red outline delineates the shallow SJB segment used to calculate moment deficit. Letters indicate the locations of asperities A & B. Grey circles are double-difference relocated earthquakes [*Waldhauser and Ellsworth*, 1999], white circles **20 km south of XSJ2** are earthquakes from the 1990 Chittenden swarm**, the white circle 10 km north of XSJ2 is the 1998 M$_w$5.1 San Juan Bautista earthquake. All seismicity symbols are scaled to the estimated rupture area given a circular slip patch and 3 MPa stress drop.** Grey stars are the projected locations of M$\geq$6 earthquakes within 5 km of the San Andreas fault surface trace from *Toppozada et al.* [2000]. **Black area signifies that no slip rate was estimated for that fault region.**
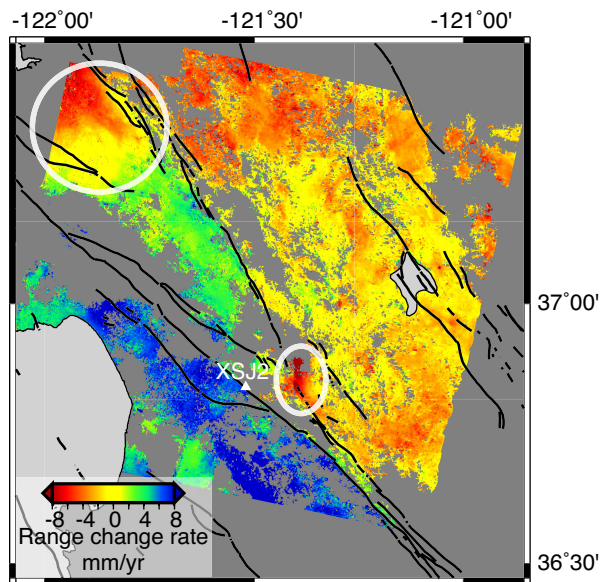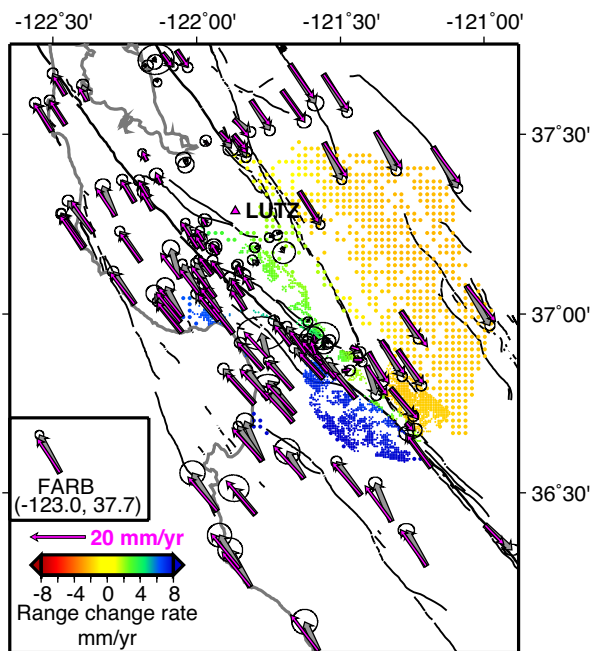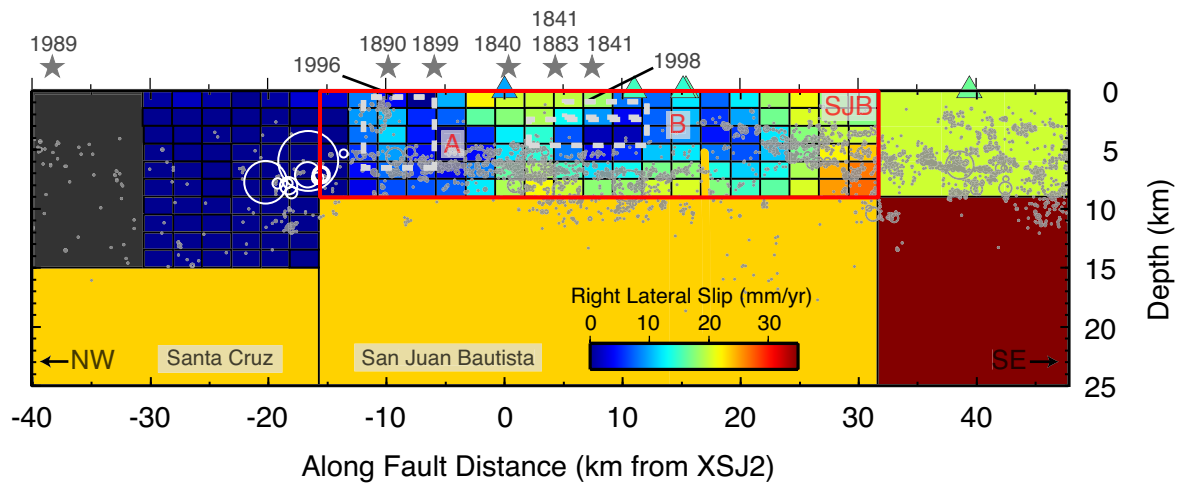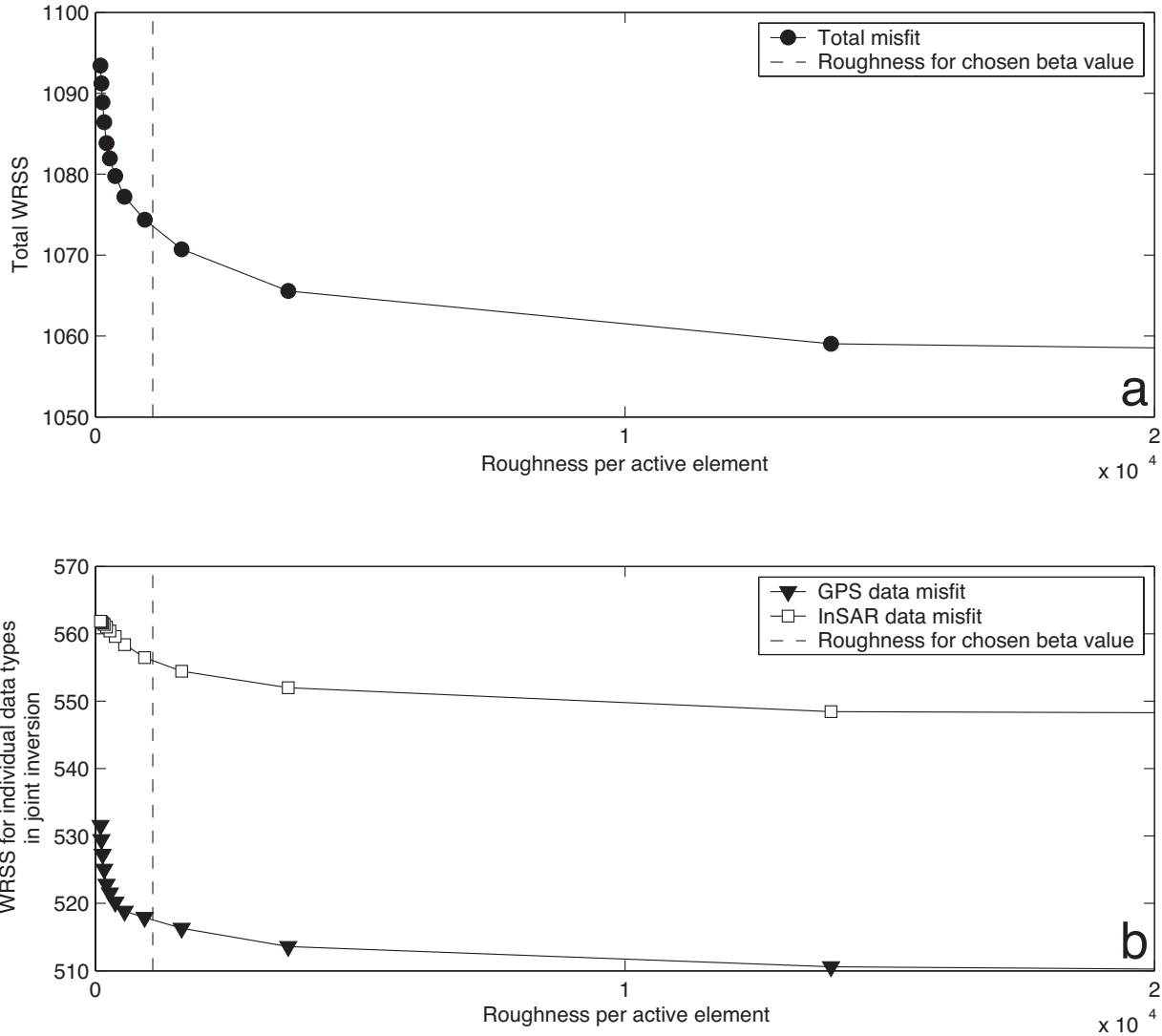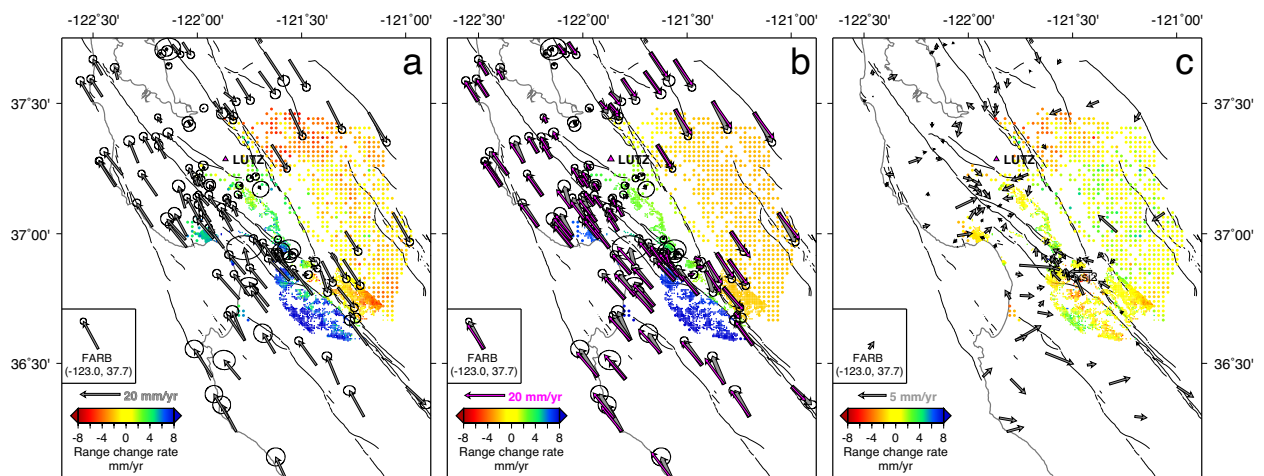
Figure 1.

Figure 2.

Figure 3.

Figure S1. In auxiliary materials: a) roughness per non-zero element on the shallow, discretized segments vs. total weighted residual sum of squares in joint inversions. b) roughness per non-zero element vs. misfit of individual data sets in the joint inversion. Dashed lines show smoothing weight (beta=186) used in this study.

Figure S2. In auxiliary materials: a) Observed InSAR range-change rate samples and GPS velocities (with 95% confidence ellipses) used in model inversion. b) Modeled range-change rate samples and GPS velocities (purple arrows) from joint inversion. Observed GPS velocities are also plotted as thick grey arrows. c) Residual range-change rate samples and GPS velocities. All GPS velocities are relative to station LUTZ (purple triangle in all figures)
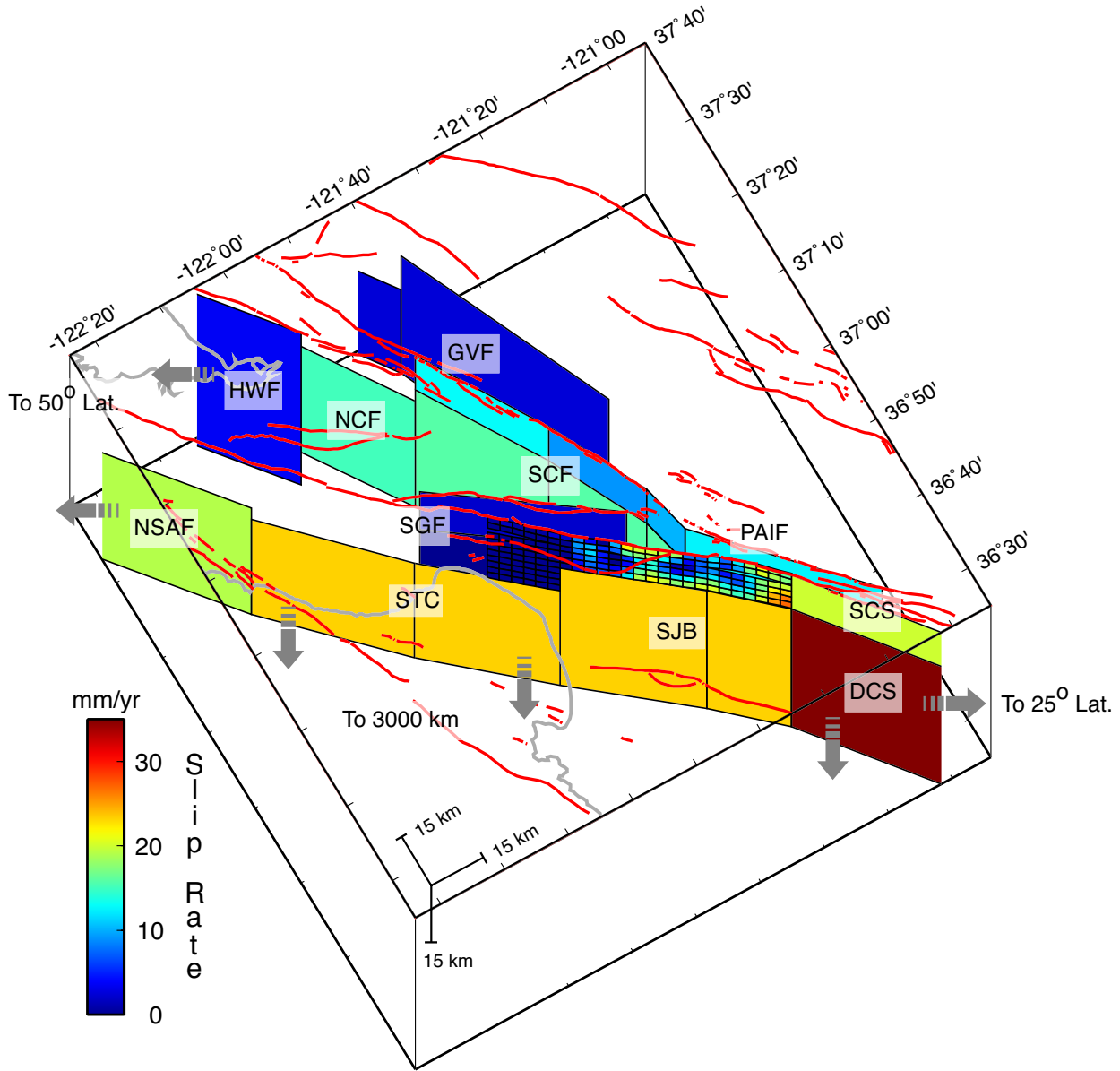
Figure S3.

Figure S3.   In auxiliary materials: 3D perspective view of modeled regional fault system and inversion results. Fault labels: SJB, San Juan Bautista segment, STC, Santa Cruz segment, DCS, Deep Creeping Section, SCS, Shallow Creeping Section, NSAF, Northern San Andreas Fault, SGF, Sargent Fault, HWF, Hayward Fault, NCF, Northern Calaveras Fault, SCF, Southern Calaveras Fault, PAIF, Paicines Fault, GVF, Green Valley Fault. Deep dislocation are extended to 3000 km depth. NSAF, HWF and NCF are extended to 50 degrees latitude and DCS and SCS are extended to 25 degrees latitude. Fault surface traces are plotted as red lines, grey lines are coast lines.